RSC Advances

PAPER

View Article Online
View Journal | View Issue

Cite this: *RSC Adv.*, 2015, **5**, 31422

Dual purpose poly(3,4-ethylenedioxypyrrole)/vanadium pentoxide nanobelt hybrids in photoelectrochromic cells and supercapacitors†

B. Narsimha Reddy,‡[a] Radha Mukkabla,‡[a] Melepurath Deepa*[a] and Partha Ghosal[b]

Received 21st March 2015
Accepted 25th March 2015

DOI: 10.1039/c5ra05015d

www.rsc.org/advances

Poly(3,4-ethylenedioxypyrrole) (PEDOP)/vanadium pentoxide (V_2O_5) nanobelt hybrid films were prepared for the first time. V_2O_5 nanobelts with a monoclinic structure were grown by a hydrothermal route and a PEDOT layer was coated onto V_2O_5 nanobelts by electropolymerization to yield the PEDOP/V_2O_5 hybrid. The hybrid showed a fourfold increment in electrical conductivity compared to the pristine oxide, and a work function of 4.71 eV (by Kelvin probe force microscopy), which was intermediate to that of PEDOP and V_2O_5. Both oxide and hybrid showed green-red luminescence. The PEDOP/V_2O_5 hybrid or V_2O_5 films were assembled into energy saving photoelectrochromic cells, by combining with a photovoltaic electrode of CdS/titania, and in response to 1 sun illumination for different durations, the hybrid showed a dynamic transmission modulation (ΔT), as it switched from a yellow to a dark green optical state, without the application of any external bias, by simply consuming the electrical current produced by the irradiated CdS/titania. The hybrid exhibited a maximum ΔT of 65.5% at 475 nm, which was greater by 82% compared to pristine V_2O_5 at the same wavelength. The ability of PEDOP to provide facile conduction pathways for fast and improved electron transfer and transport in the PEDOP/V_2O_5 hybrid, enhances the optical contrast produced. The versatility of the hybrid was established by assembling asymmetric supercapacitors with the hybrid or polymer or oxide and a liquid electrolyte. The synergistic effects of PEDOP (high electrical conductivity) and V_2O_5 nanobelts (large surface area) and their ability to store/release charge by undergoing reversible Faradaic reactions were reflected in a high specific capacitance of 224 F g^{-1} delivered by the hybrid, higher by 83% and 69% relative to pristine V_2O_5 and PEDOP. The hybrid shows an energy density of 223 W h kg^{-1} at a power density of 3.8 kW kg^{-1}, and an acceptable cycling performance with 90% capacitance retention after 5000 cycles. The PEDOP/V_2O_5 hybrid is useful for advanced next-generation self-powered electrochromic smart windows and supercapacitors.

1. Introduction

Transition metal oxides such as WO_3, MoO_3, NiO_x, IrO_2 *etc.* owing to their ability to exist in two or more oxidation states enables their widespread usage in diverse applications. Typical applications range from energy saving electrochromic devices, wherein a current or voltage input to the oxide induces an optical change, or energy conversion devices, wherein they are employed as a hole transport layer in organic solar cells,[1] or as a wide gap semiconducting support in dye sensitized solar cells[2] or in energy storage devices as electrode materials in pseudocapacitors or lithium ion batteries,[3,4] wherein they store energy by intercalation or deintercalation of ions through redox reactions. Among various oxides, vanadium pentoxide (V_2O_5) is a well-established intercalation compound due to a layered crystalline structure and has been used in the past as an electrochromic material and also as an electrode for supercapacitors and in Li ion batteries.[5–7] All these applications of V_2O_5 rely on its ability to intercalate and deintercalate charge by undergoing oxidation and reduction reactions. Nanostructures of V_2O_5 (rods, belts, wires, sheets) have been utilized in the literature, owing to the higher surface area offered by these morphologies compared to the particulate structure.[8–11] V_2O_5 nanostructures can easily entrap inorganic/organic cations from the electrolyte and release them under a need basis, under an appropriate stimulus, a property, which is exploited in electrochromic, pseudocapacitor and Li-ion battery applications. However, the electronic conductivity of V_2O_5 is low, which leads to sluggish ion

[a]*Department of Chemistry, Indian Institute of Technology Hyderabad, Ordnance Factory Estate, Yeddumailaram-502205, Telangana, India. E-mail: mdeepa@iith.ac.in; Fax: +91-40-23016003; Tel: +91-40-23016024*

[b]*Defence Metallurgical Research Laboratory, DRDO, Hyderabad-500058, Telangana, India*

† Electronic supplementary information (ESI) available: Table of solar cell efficiencies. See DOI: 10.1039/c5ra05015d

‡ Both authors contributed equally to the work.

insertion/extraction rates.[12] Approaches to alleviate this issue involves the formation of hybrids using electrically conducting polymers such as poly(3,4-ethylenedioxythiophene) or PEDOT[13] or carbon nanostructures. In an earlier report,[14] PEDOT nanoribbons interspersed between V_2O_5 layers were prepared by a microwave irradiation route and authors demonstrated a higher discharge capacity for the composite relative to pristine V_2O_5 in a Li-ion battery.[14] In another study, a V_2O_5–poly(aniline) or PANI hybrid was synthesized by a layer-by-layer assembly method and authors obtained superior performances in terms of electrochromic contrast and charge storage capacity for the hybrid.[15] In yet another notable study, a V_2O_5 gel was assembled into a solid state cell by ink jet printing and the gel switched between green, yellow and blue hues and could sustain 30 000 cycles with only 18% transmittance loss.[16] A composite of V_2O_5 nanoparticles embedded in reduced graphene oxide nanosheets was prepared by a hydrothermal route and it exhibited a specific capacitance of 537 F g^{-1} (at 1 A g^{-1}) in an aqueous electrolyte, which was found to be greater than that of pure V_2O_5 microspheres.[17] A V_2O_5–poly(pyrrole) (PPy) composite exhibited good charge-storage properties over a large potential window of ~2 V, with a high specific capacitance.[18] A cucumber-like MnO_2 nanoparticles enriched V_2O_5/PEDOT coaxial nanowires heterostructured material exhibited enhanced electrochemical cycling performance.[19] In another study, carbon black anchored V_2O_5 nanobelts were synthesized and the former improved the structural stability to cycling, increased ionic diffusivity and electronic conductivity, thus resulting in a larger specific capacity, when used as a cathode in a Li-ion battery.[20] Of the conducting polymers which have been used in the past for constructing supercapacitors, such as PEDOT,[21] PANI,[22] PPy,[23] the pyrrole analogue of PEDOT, poly(3,4-ethylenedioxypyrrole) (PEDOP) has rarely been used for energy storage applications,[24,25] despite a lower oxidation potential than PEDOT (−0.5 V compared to −0.25 V *versus* Ag/Ag^+), an outstanding stability and an inertness to the adverse effects of air and atmosphere.[26] These attributes render PEDOP to be an ideal choice for designing stable, conductive electrodes for pseudocapacitor applications.

In the present study, V_2O_5 nanobelts were synthesized by a hydrothermal route and the electrical conductivity of the oxide was improved by an integration with PEDOP. PEDOP is also a cathodically coloring electrochrome, as it switches between pale blue and red states, upon application of oxidative and reductive electric potentials, but here we used an optimal thickness for PEDOP, thick enough to serve as an electron conduit and thin enough to not show a noticeable color change, similar to the role played by PEDOT:PSS (poly(styrene sulfonate)) in an organic solar cell,[27] wherein PEDOT:PSS only shuttles holes without undergoing any color transition. A yet unreported PEDOP/V_2O_5 hybrid was synthesized by electrophoretically depositing a V_2O_5 layer on an electropolymerized PEDOP film. Pristine V_2O_5 and PEDOP/V_2O_5 electrodes were used for constructing photoelectrochromic cells (PECs), wherein an inexpensive CdS/TiO_2 was used as the photoactive electrode and the hybrid/oxide was employed as the electrochromic counter electrode separated by an electrolyte. In a PEC, upon illumination, the photocurrent produced by the photoanode is channelized to the counter electrode *via* the external circuit and the oxide based electrode undergoes color change upon reduction. To date, there are no reports on the use of either V_2O_5 or a PEDOP/V_2O_5 hybrid as photoelectrochromic electrodes in a quantum dot based solar cell. Further, most of the reports on PECs, typically employ a dye sensitized photoactive electrode to color the electrochromic electrode.[28–30] In addition, the ability of V_2O_5 or PEDOP or the PEDOP/V_2O_5 hybrid to function as a pseudocapacitive electrode is also demonstrated by assembling them into asymmetric supercapacitor cells followed by an evaluation of their electrochemical properties. The structural and electrical properties of the electrodes are correlated with their photoelectrochromic and charge storage characteristics. We demonstrate the ability of the PEDOP/V_2O_5 hybrid to function as an optical color switching electrode in a PEC cell, and as an excellent ion storage electrode in a supercapacitor.

2. Experimental

2.1. Chemicals

3,4-Ethylenedioxypyrrole (EDOP), lithium perchlorate ($LiClO_4$, purity > 98%), sodium vanadate (Na_2VO_4), Triton-X, titanium tetrachloride ($TiCl_4$) and graphite powder (particle size < 20 μm) were purchased from Sigma-Aldrich. Sodium chloride (NaCl), hydrochloric acid (HCl), cadmium acetate ($Cd(CH_3COO)_2$), sodium sulfide (Na_2S), acetonitrile, *N*-methyl pyrrolidine (NMP), propylene carbonate (PC), and acetone were obtained from Merck. TiO_2 (P25) nanopowder was a free gift from Evonik. Ultrapure water (~18.2 MΩ cm) or deionized water (DIW) was obtained through a Millipore Direct-Q3 UV system. SnO_2 : F (FTO) coated glass substrates with a sheet resistance of about 14 Ω sq^{-1} were procured from Pilkington, washed with soap solution, flushed with large amounts of distilled water and cleaned with acetone before use.

2.2. Synthesis of PEDOP films and V_2O_5 nanobelts

A clear solution of 0 3,4-EDOP (0.1 M) and $LiClO_4$ (0.1 M) in acetonitrile (20 mL) was prepared for fabricating PEDOP films. Electropolymerization of films was performed in a three electrode configuration. FTO coated glass plates were employed as working and counter electrodes, and an Ag/AgCl/KCl cell was used as the reference electrode. Bluish-black colored films of perchlorate doped PEDOP films were deposited under potentiostatic conditions at room temperature in chronoamperometric mode by application of +1.5 V to the working electrode for 500 s. The films were washed in deionized water, dried in air for 2 h and stored in air.

V_2O_5 nanobelts were synthesized using a hydrothermal method. A solution of Na_2VO_4 (2.5 mmol) was prepared in deionized water (20 mL). NaCl (0.02 mol) used as capping agent was added to above solution. The resulting solution was stirred for 10 min. The pH of the solution was adjusted to 2 by adding 3 M HCl in a drop-wise manner. This solution was further

stirred for another 10 min and then transferred to a 50 mL Teflon lined autoclave and heated at 180 °C for 12 h. A yellow colored precipitate was formed at the bottom of autoclave. The precipitate was cleaned with plenty of deionized water, dried in an oven and used for preparing pristine V_2O_5 and hybrid films.

2.3. Preparation of V_2O_5 and PEDOP/V_2O_5 films

V_2O_5 powder (~1 g) was transferred to a mortar and grinded for a few minutes along with a few drops of NMP. A homogeneous deep yellow-brown colored paste of V_2O_5 was obtained and it was diluted with NMP (10 mL) and ultrasonicated for 10 min. The suspension was used in an electrophoresis cell, with two FTO coated glass plates as electrodes and potential of 20 V was applied for 3 min. Using a Tarsons MC-01 electrophoresis power supply. A deep yellow colored deposit of V_2O_5 was obtained on one of the FTO substrates. For preparing the PEDOP/V_2O_5 hybrid, one of the two FTO coated substrates was replaced by a V_2O_5 film, and a bluish yellow deposit was obtained, upon application of +1.5 V for 500 s in a monomer-salt bath. The films were washed in acetonitrile, dried and stored in air.

2.4. Construction of solar cells and supercapacitors

A TiO_2 coating was made on FTO/glass by doctor blading from a paste of TiO_2 powder prepared in ultrapure water (8 mL) and Triton X-100 (20 mg). The TiO_2 film was annealed at 500 °C for 30 min. The resulting film was kept immersed in an aqueous $TiCl_4$ (40 mM) solution for 30 min at 70 °C. The TiO_2 film was rinsed in distilled water and sintered at 500 °C for 30 min, cooled to ambient temperature and used for CdS deposition. CdS quantum dots (QDs) were deposited on the TiO_2 coated glass electrodes by successive ionic layer absorption and reaction (SILAR) method. The TiO_2/FTO electrode was sequentially immersed in four different beakers for about 30 s immersion time, in each solution. The first dipping solution contained aqueous $Cd(CH_3COO)_2$ (0.1 M) which, was followed by an ultrapure water rinse to remove superfluous acetate. The film was then immersed in aqueous Na_2S (0.1 M), and again followed by a water dip to remove the surplus sulfide. The immersion cycle was repeated ten times. The resulting films were yellow and were referred to as CdS/TiO_2 electrodes. Quantum dot solar cells or photoelectrochromic cells were assembled by using a CdS/TiO_2 electrode as the photoanode, a PEDOP or V_2O_5 or PEDOP/V_2O_5 as the counter electrode and aqueous Na_2S (0.1 M) as the electrolyte.

A dispersion of graphite (0.1 g) in ethanol (30 mL) was prepared by ultrasonication for 15 min and using a two electrode configuration with FTO coated glass as the two electrodes. Graphite coatings were obtained on one of the electrodes upon application of a constant potential of 20 V for 5 min using an electrophoresis power supply. Graphite electrodes have been labeled as Gr in this study. An acrylic tape of 0.5 mm thickness was employed as the spacer and was applied along the four edges of the active electrode (V_2O_5 or PEDOP or PEDOP/V_2O_5), the liquid electrolyte (1 M $LiClO_4$ in PC) was filled in the cavity and heated in a vacuum oven at 50 °C till a bubble free electrolyte layer was obtained. The counter electrode (Gr) was then pressed upon this assembly and the whole configuration was held together using binder clips and placed in an online vacuum oven for 1 h. The edges were finally sealed with an epoxy. The active material loading on the current collector was maintained in the range of 1.2 to 1.5 mg.

2.5. Instrumental methods

Raman spectra were recorded for the electrodes on a Bruker Senterra Dispersive Raman microscope spectrometer; the laser excitation wavelength was fixed at 785 nm. X-ray diffraction patterns were recorded on a XRD, PANalytical, X'PertPRO instrument with Cu-Kα (λ = 1.5406 Å) radiation. Surface morphology analysis was performed using a field emission scanning electron microscope (Carl Zeiss Supra 40 FE-SEM). Transmission electron microscopy (TEM, model Tecnai G2, FEI operating an accelerating voltage of 200 kV) was carried out by dispersing samples in toluene, and then transferring them onto carbon coated copper grids. Thermogravimetric analysis (TGA TA instruments, Q600) was carried out on the hybrid to calculate the amount of PEDOP in the hybrid. Atomic force microscopy (AFM), and Kelvin probe force microscopy (KPFM) measurements were performed on the electrodes using a Veeco, Multimode 8 with Scan Asyst (Nanoscope 8.10 software) microscope. The conductive probes used in this study were coated with platinum–iridium on front and back sides. The probe tip had a radius of 10 nm, spring constant of 0.2 N cm^{-2}, a current sensitivity of 1 nA V^{-1}. For KPFM, the sample deposited on FTO coated glass (area ~9 mm^2) was affixed on a stainless steel disk with a conducting carbon tape. A thin strip of pin-hole free silver paste was used for taking contacts. Optical transmittance *versus* wavelength plots were measured for the electrochromic electrodes (V_2O_5 or PEDOP/V_2O_5) after different time spans of 1 sun illumination, a Shimadzu UV-Visible-NIR 3600 spectrophotometer. The optical absorption spectra of the films were measured in the diffuse reflectance mode and converted to absorbance using Kubelka Munk function on the same instrument. Galvanostatic charge–discharge measurements were performed on a battery testing unit (Arbin Instruments, BT 2000) at different current densities over a voltage span of ~2 V, in a two-electrode cell configuration. The mass values for the films were determined with a Sartorius microbalance CPA2P with a 1 μg resolution. Photoluminescence (PL) spectra of films were measured on a Horiba Flouromax-4 fluorescence spectrometer; a suitable filter was utilized during the measurement and background correction was also applied. Electropolymerization, cyclic voltammetry and chronoamperometry were done on an Autolab PGSTAT 302N potentiostat/galvanostat equipped with a NOVA 1.9 software. *I–V* characteristics of the solar cells were measured using a Newport Oriel 3A solar simulator with a Keithley model 2420 digital source meter. A 450 W Xenon arc lamp with an irradiance of 100 mW cm^{-2} of Air Mass (AM) 1.5 was used as the light source; the spatial uniformity of irradiance was confirmed by calibrating with a 2 cm × 2 cm Si Reference Cell and re-confirmed with a Newport power meter.

3. Results and discussion

3.1. Structural analysis

FE-SEM images of pristine V_2O_5, PEDOP and PEDOP/V_2O_5 hybrid at different magnifications are shown in Fig. 1. As can be judged from Fig. 1a–c, pristine V_2O_5 has a predominant nanobelt like morphology; we refer to them as belts and not rods, as they are curved in some regions. The lengths of the belts extend over several tens of microns, and their widths lie in the range of 50 to 70 nm. The nanobelts are misaligned with respect to each other and they are overlapping. Upon coating the polymer, the resulting PEDOP/V_2O_5 hybrid continues to retain the nanobelt like morphology (Fig. 1e and f), but the belts tend to aggregate, suggestive of the conducting polymer serving as glue which connects the V_2O_5 belts, which is advantageous for improving the electronic conductivity of the whole system. The porosity of the pristine V_2O_5 is such that it allows an intimate contact between the V_2O_5 nanobelts and PEDOP during hybrid formation and therefore it is not just the uppermost layer but the entire cross-section of belts which PEDOP can anchor onto. Since there are no particles seen in the low magnification image of the composite, it is apparent that despite the polymer coating, the advantage of the elongated shapes such as high surface area which enables increased ion uptake from the electrolyte during electrochemical switching can be exploited. The SEM image of the pristine polymer shows a granular porous structure. The EDX plot of V_2O_5 shows two dominant signals from oxygen and vanadium, and that of PEDOP shows signals from C, N and O. The EDX plot of PEDOP/V_2O_5 shows signals from C, N, O and V, indicating the inclusion of the polymer in V_2O_5.

The X-ray diffractograms and the Raman spectra of pristine V_2O_5 nanobelts, PEDOP and PEDOP/V_2O_5 hybrid are shown in Fig. 2a and b respectively. The XRD pattern of V_2O_5 shows prominent diffraction peaks at $d = 7.44$, 3.47, 3.1, 2.9 and 1.8 Å which correspond to $(\bar{2}01)$, (500), $(\bar{1}12)$, $(\bar{6}01)$ and $(\bar{1}21)$ planes of the monoclinic crystal structure of V_2O_5, in concurrence with JCPDS file number 07-0332. Additional peaks with relatively lower intensities were also observed, and these were also indexed to the diffraction lines of monoclinic V_2O_5. The XRD pattern of pristine PEDOP shows a broad hump in the low 2θ region, characteristic of anamorphous structure, which is typical trait of conducting polymers. The pattern of PEDOP/V_2O_5 hybrid, shows the same peaks at the d-values corresponding to the monoclinic structure of V_2O_5, thus indicating the crystal structure of V_2O_5 is not impacted, upon coating with the polymer. The Raman spectrum of pristine V_2O_5 nanobelts show broad peaks at 763 and 472 cm^{-1} corresponding to the vibrational stretching modes of V–O linkages. A cluster of peaks is also seen at ~296 and 256 cm^{-1} which are assigned to the bending vibrational modes of V=O bonds. An intense peak observed at ~130 cm^{-1} is attributed the lattice vibrations. The Raman spectrum of pristine PEDOP shows a doublet of intense peaks at 1637 and 1584 cm^{-1}, which are ascribed to the asymmetric C=C stretching vibrations, followed by another set of twin peaks at 1427 and 1393 cm^{-1} corresponding to the symmetric C_α=C_β(–O) stretching and C_β–C_β stretch modes. An intense peak is also seen at 1202 cm^{-1} which arises from overlapping modes of C_α–$C_{\alpha'}$ (inter-ring stretching) and C_β–H bending vibrations. The PEDOP/V_2O_5 hybrid shows peaks from both V_2O_5 and PEDOP, slightly shifted with respect to the pristine moieties, thus confirming the formation of the hybrid. In the hybrid, three peaks cloistered with apexes at 1637, 1615 and 1585 cm^{-1} originate from the ν_{asym}(C=C) modes of PEDOP, a broad peak at 1415 cm^{-1} corresponds to C_α=C_β(–O) stretching vibration of PEDOP and the peak at 1193 cm^{-1} is due to the $\nu(C_\alpha–C_{\alpha'}) + \delta(C_\beta–H)$ modes. Strong, intense broad peaks are also observed at 762 and 470 cm^{-1} due to ν(V–O) stretch modes of V_2O_5 nanobelts. Peaks at 294 and 262 cm^{-1} correspond to δ(V=O) modes and the peak at 142 cm^{-1} arises from lattice vibrational modes of V_2O_5, thus re-affirming the hybrid formation.

The transmission electron microscopy (TEM) images of pristine V_2O_5 (Fig. 3a and b) also reveal that V_2O_5 has a nanobelt structure with flat and smooth surfaces, and widths in the range of 10 to 100 nm. The nanobelts are overlapping and are of varying lengths. The corresponding lattice scale image (Fig. 3c) shows an inter-fringe spacing of 0.67 nm and this matches with the 200 reflection of monoclinic V_2O_5. The selected area electron diffraction (SAED) pattern (Fig. 3d(i)) from the pristine nanobelts shows a spotty pattern and the spots were indexed to the (200) and $(\bar{3}03)$ reflections of monoclinic V_2O_5, as per JCPDS: 07-0332. The microstructure of pristine polymer (Fig. 3e) shows the polymer to have a featureless morphology, as small

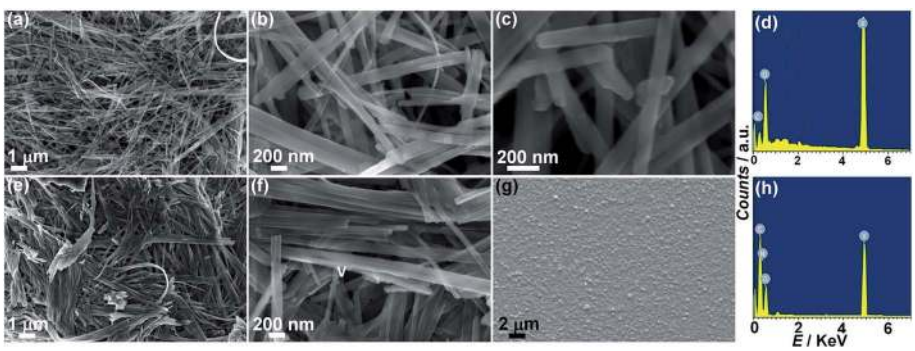

Fig. 1 FE-SEM micrographs of (a–c) pristine V_2O_5 nanobelts and (e and f) PEDOP/V_2O_5 hybrid at different magnifications and (g) pristine PEDOP; (d and h) EDX plots of pristine V_2O_5 nanobelts and PEDOP/V_2O_5 hybrid respectively.

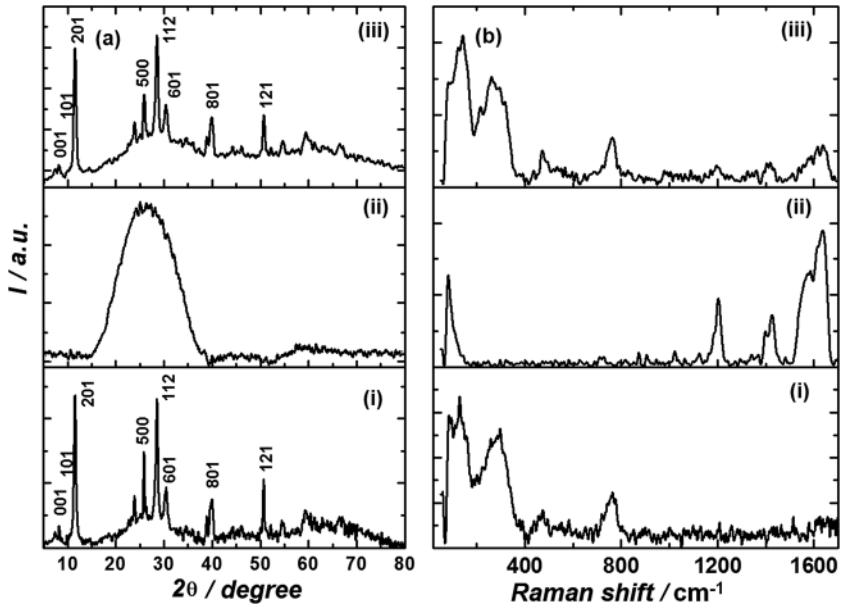

Fig. 2 (a) XRD patterns and (b) Raman spectra of: (i) V_2O_5, (ii) PEDOP and (iii) PEDOP/V_2O_5 hybrid. The planes 201, 112, 601, 801 and 121 have bars on the *h*-values.

interlinked particles with indistinctive grain boundaries are seen which is typical of conducting polymers. The TEM images of the PEDOP/V_2O_5 hybrid (Fig. 3f and g) show the belt like shapes to be enveloped in a sheath of the conducting polymer PEDOP. The dark domains in the images arise from the polymer which is enmeshed with the V_2O_5 nanobelts. The SAED pattern extracted from the irregular shaped structures in the hybrid, shows diffuse rings characteristic of the amorphous nature of PEDOP (Fig. 3d(iii)). The SAED pattern from the belt like shape shows bright spots superimposed over diffuse rings, wherein the bright spots are due to the crystalline plane facets of V_2O_5 (Fig. 3d(ii)). In the hybrid, the polymer PEDOP is thoroughly mixed with the V_2O_5 belts for they are hardly visible as discrete entities in the images. The interfacial contact between the polymer and V_2O_5 appears to be almost Ohmic, for no grain boundaries are perceptible. This implies that doped PEDOP, being intrinsically electronically conducting and being in intimate contact with one-dimensional V_2O_5 nanobelts, can provide efficient electron transport pathways, during electrochemical charge insertion and extraction, which can increase the ion uptake capability of V_2O_5 nanobelts and also help in minimizing the Ohmic drop across the cell. TGA analysis was also performed on the PEDOP/V_2O_5 hybrid (Fig. S1, ESI†), and the proportion of PEDOP in the hybrid was deduced to be 46% by weight. This implies that the V_2O_5 content is the hybrid is ~54% by weight.

3.2. Conductivity and photoluminescence (PL) of films

The *I–V* characteristics of pristine V_2O_5 nanobelts, PEDOP and PEDOP/V_2O_5 hybrid are displayed in Fig. 4a. A spring contact probe was used to ensure that there was no puncturing of the

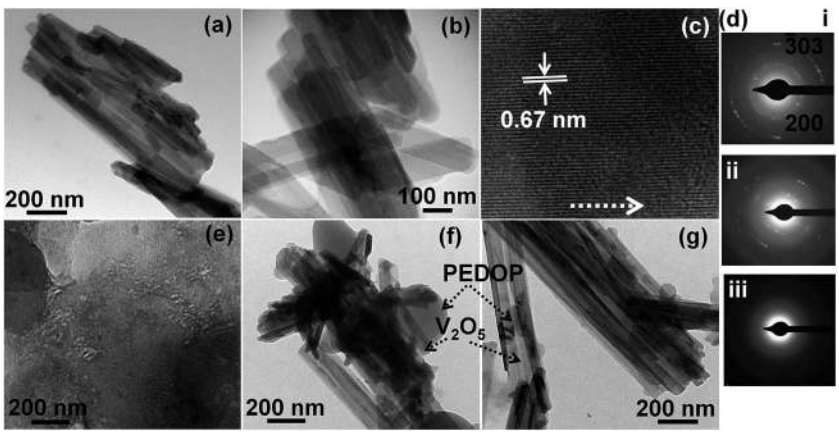

Fig. 3 TEM images of (a and b) pristine V_2O_5 nanobelts, (c) lattice scale image of V_2O_5, (e) pristine PEDOP and (f and g) PEDOP/V_2O_5 hybrid. (d) SAED patterns obtained from the (i) pristine V_2O_5 nanobelts and of the hybrid: (ii) from V_2O_5 and (iii) from the polymer parts respectively.

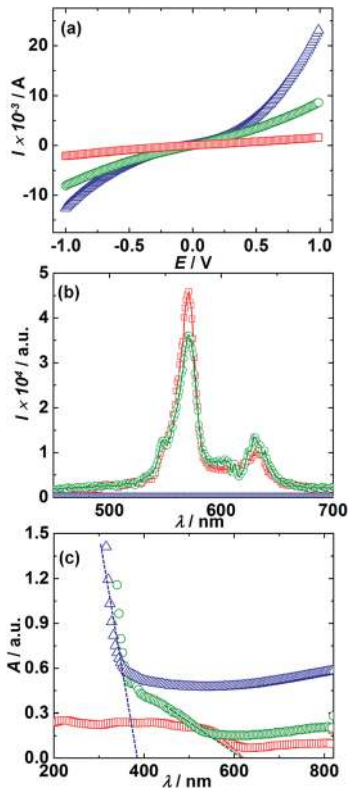

Fig. 4 (a) LSV (recorded in FTO/sample/SS configuration)-, (b) PL- and (c) absorption-plots of pristine V_2O_5 nanobelts (□), pristine PEDOP (△) and PEDOP/V_2O_5 hybrid (○). The points of intersection of dashed lines with the abscissas in (c) represent the optical band gaps.

film during the measurement. The films show linear variation of current with potential with different slopes in different domains of the −1 to +1 V measurement range at room temperature. The conductivities were calculated from the slopes using $\sigma = (I/V) \times d/A$, and averaged for a given film, where d is the thickness of the film and A is the area of contact of the probe with the film. Film thicknesses (d) were measured by running an AFM tip across a step of FTO/film, and from the height profile, the thickness was determined. Pristine V_2O_5 nanobelts, PEDOP and PEDOP/V_2O_5 hybrid show thicknesses of about 610, 600 and 570 nm respectively. Pristine V_2O_5 film exhibits the lowest current response in comparison to PEDOP and PEDOP/V_2O_5 hybrid in the same potential range, for the same geometric area and film thickness. As expected, pristine PEDOP exhibits the highest conductivity of 3.6 mS cm^{-1} and the conductivity of the PEDOP/V_2O_5 hybrid is slightly lower (1.6 mS cm^{-1}). Conductivity of pristine V_2O_5 is the least (0.4 mS cm^{-1}), for the conductivity is largely due to the defect states, and their concentration is small, not enough to induce a significant increase in the electronic conductivity. Since the conductivity of the PEDOP/V_2O_5 hybrid is 4 times larger than that of pristine oxide, it is obvious that the polymer is effective in improving the electron conduction capability of V_2O_5. The photoluminescence and absorption plots of V_2O_5, PEDOP and PEDOP/V_2O_5 are shown in Fig. 4b and c respectively. Two peaks are observed at 571 and 634 nm for V_2O_5 and PEDOP/V_2O_5. The latter peak corresponds to radiative transitions between the energy states which are introduced within the band gap due to oxygen defects. The optical band gap of V_2O_5 nanobelts deduced from the absorption edge is 2.02 eV. It is the difference between the bottom of the V3d conduction band and the top of the O2p valence band. Since the higher intensity PL peak is observed at a slightly higher energy of 2.17 eV, it is probably due to electronic transitions, between the top of the V3d conduction band and the bottom of the O2p valence band. Pristine PEDOP does not show any PL, and the hybrid shows a PL response, almost similar to that V_2O_5 and the band gap is also unchanged in the hybrid, thus indicating that PEDOP does not alter the electronic structure of V_2O_5. Oxygen vacancies are the most commonly found defects in solution processed oxides, and the band gap of V_2O_5 has been observed to lie in the range of 1.95 to 2.4 eV,[31] which matches with the value observed herein. Previously, for V_2O_5 nanorods prepared by a thermal advanced process, deconvoluted PL peaks in the visible region at 650 and 730 nm were observed.[32] In another study, broad chemiluminescence peaks within the energy range of 1.5 to 3.6 eV were observed for V_2O_5 nanorods, grown by a controlled thermal treatment process.[31] The ability of V_2O_5 nanobelts, prepared herein, to exhibit green-red luminescence, can be of use in light emitting devices.

3.3. Surface potential studies

KPFM was used for studying the surface potential profiles and for the determination of work functions of V_2O_5 nanobelts, PEDOP and the PEDOP/V_2O_5 hybrid. KPFM measures the contact potential difference (V_{CPD} or surface potential) between a conducting Pt/Ir tip and the sample surface and it is given by the following equation.

$$V_{CPD} = \phi_{tip} - \phi_{sample}/e^- \quad (1)$$

In (1) ϕ_{tip} and ϕ_{sample} are the work functions of the tip and the sample, and e^- is the electronic charge. When an AFM tip is brought close to the sample surface, an electrical force is generated between the tip and sample surface, due to the differences in their Fermi energy levels. Upon electrical contact, the Fermi levels align through electron current flow, the system equilibrates and a V_{CPD} acts between the tip and the sample. A V_{DC} equal and opposite to V_{CPD} is applied to nullify the latter. A V_{AC} is applied along with V_{DC} which enables the determination of the sample work function *via* V_{CPD}. V_{CPD} is the work function difference between the tip and the sample, and since the work function of the tip is known, ϕ_{sample} can be determined from (1). The topography and the corresponding surface potential maps of V_2O_5 nanobelts, PEDOP and the PEDOP/V_2O_5 hybrid are shown in Fig. 5. The work function of the Pt/Ir tip was initially calibrated with highly ordered pyrolytic graphite (HOPG) which has a fixed work function of 4.6 eV and this value was used to convert the measured V_{CPD} to the absolute surface work function. The magnitude of ϕ_{sample} is given by:

$$\phi_{sample} = 4.6 \text{ eV} + V_{CPD(HOPG)} - V_{CPD(sample)} \quad (2)$$

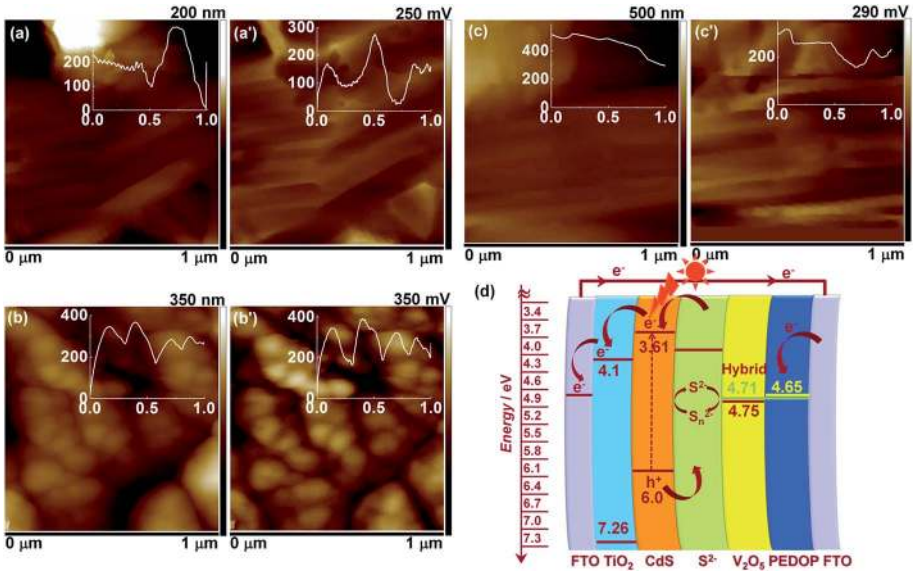

Fig. 5 Topography and surface potential maps of (a and a′) V_2O_5 nanobelts, (b and b′) PEDOP and (c and c′) PEDOP/V_2O_5 hybrid, recorded over scan areas of 1 μm × 1 μm. Insets of a–c and a′–c′ are the corresponding section profiles, obtained from the images. (d) Energy band diagram of a quantum dot solar cell with a CdS/TiO_2 as the photoanode, an aqueous solution of 0.1 M Na_2S as electrolyte and V_2O_5 or PEDOP or PEDOP/V_2O_5 hybrid as counter electrode.

Here, $V_{CPD(sample)}$ was obtained from the surface potential maps taken over a scan area of 1 μm × 1 μm, for each sample. $V_{CPD(HOPG)}$ was experimentally determined to be 400 mV, and $V_{CPD(sample)}$ for V_2O_5 nanobelts, PEDOP and the PEDOP/V_2O_5 hybrid were 250, 350 and 290 mV respectively, for the same value of tip-sample separation of 50 nm. The work functions of V_2O_5 nanobelts, PEDOP and the PEDOP/V_2O_5 hybrid were calculated to be 4.75, 4.65 and 4.71 eV. The impact of work function is discussed in the next section.

3.4. Photoelectrochromic response

Photoelectrochemical cells were constructed with CdS/TiO_2 as the photoanode, 0.1 M Na_2S as the electrolyte and pristine V_2O_5 or PEDOP or the PEDOP/V_2O_5 hybrid as the counter electrode. The *J*–*V* characteristics were measured under one sun (100 mW cm^{-2}) irradiance and are displayed in Fig. 6. The energy band diagram illustrating the valence and conduction band positions of the various components of the solar cell are shown in Fig. 5d. The positions for TiO_2, CdS and S^{2-} were used from our previous report.[33] Upon illumination, electron–hole pairs are generated in the photoactive CdS layer, and electrons are injected from the conduction band of CdS to the conduction band of TiO_2 and then to the current collector (FTO). A low concentration of CdS is maintained to keep the device transparent. The electrons reach the counter electrode *vis-à-vis* the external circuit. As in a conventional electrochromic device, the injection of sodium ions into the electrochromic layer causes it to color. Here, if pristine V_2O_5 or the hybrid is used as the counter layer, it will color according to following equation.

$$\underset{\text{(Yellow, Oxidized)}}{V_2^{V}O_5} + xNa^+ + xe^- \leftrightarrow \underset{\text{(Green, Reduced)}}{Na_xV_2^{V,IV}O_5} \quad (3)$$

Electrons are transferred to V_2O_5 (in the oxidized state) from the external circuit and Na^+ ions are inserted from the electrolyte for charge compensation; the yellow film turns green upon reduction. When sunlight is blocked or in dark, the charge stored in the electrochromic layer drives the process in reverse, releasing sodium ions from the electrochromic layer and triggering it to bleach. Thus, without an external control (in closed circuit), the photoelectrochromic device will color in sunlight and bleach in its' absence. The external circuit can also be employed to control the device, disconnection of the circuit will cause the device to remain in its current state irrespective of the presence or absence of sunlight. Moreover, an external voltage can be supplied to the device to drive the device to either the bleached or colored state. A typical configuration of a photoelectrochromic device, based on CdS/TiO_2 and V_2O_5 or PEDOP/V_2O_5 is shown in Fig. 7. PEDOP is also a cathodically coloring

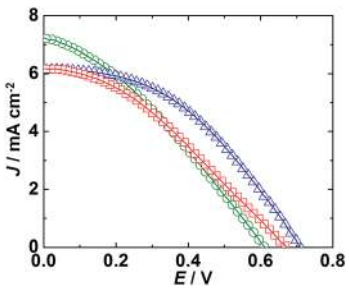

Fig. 6 *J*–*V* characteristics of solar/photoelectrochromic cells with pristine V_2O_5 nanobelts (□), pristine PEDOP (△) and PEDOP/V_2O_5 hybrid (○) as counter electrodes under one sun illumination (λ > 300 nm, 100 mW cm^{-2}, AM1.5). A CdS/TiO_2 assembly was used as the photoanode and a 0.1 M Na_2S solution was employed as electrolyte.

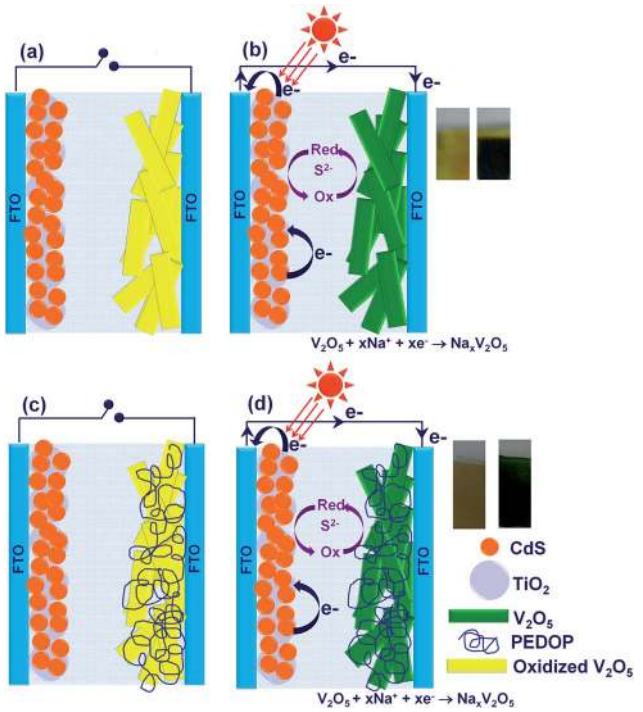

Fig. 7 Photoelectrochromic cell configurations with (a and b) pristine V_2O_5 nanobelts and (c and d) PEDOP/V_2O_5 hybrid as the coloring counter electrodes. (a and c) show the electrochromes in their bleached (yellow, oxidized) states in dark or in light under open circuit and (b and d) show the electrochromes in their colored (reduced, green) states under illumination under closed circuit. Panels on right side show the photographs of the corresponding films in bleached and colored states.

electrochrome, but here the PEDOP film thickness or concentration is optimum, enough to enhance the electrical conductivity of V_2O_5, but at the same time (even when used in its' pristine form), insufficient to undergo a perceptible color transition.

The transmittance *versus* wavelength curves, obtained for the pristine V_2O_5 nanobelts and PEDOP/V_2O_5 hybrid films when used as counter electrodes with CdS/TiO_2 photoanodes, in a photoelectrochromic cell configuration, under different durations of one sun illumination are shown in Fig. 8. The time spans for which the device was subjected to 100 mW cm^{-2} light irradiance were fixed at 10, 20, 40, 50, 60 and 70 s. No external bias was applied to the cell during the measurement. The transmittance of the film was measured at the end of each of these time intervals over the visible region from 400 to 800 nm and over the near infrared (NIR) wavelength range of 1000 to 1900 nm. The films, be it V_2O_5 or the hybrid showed excellent open circuit memory upon coloration by illumination (~3–4 h without color fading) and therefore %T plots were recorded easily under *ex situ* conditions. Prior to exposure to one sun, the film (either V_2O_5 or PEDOP/V_2O_5) was oxidized and its' transmittance in this bleached state was found to lie in the range of 75 to 80% in the visible and NIR regions. Upon illumination, the transmittance of the electrochromic film decreased as a function of increasing period of illumination. Transmission modulation (ΔT) is a useful parameter for determining the suitability of a given material for electrochromic application. We define modulation as $\Delta T(\lambda) = T_b(\lambda) - T_c(\lambda)$, where T_b and T_c are transmittances in the bleached (as-fabricated) and colored (upon x min exposure of 1 sun illumination, $x = 0$, 10, 20, 40, 50, 60 and 70 s) states respectively. Transmission modulation as a function illumination time is displayed in Fig. 9 for both V_2O_5 and PEDOP/V_2O_5 films. Transmission modulation offered by the PEDOP/V_2O_5 film for maximum contrast (achieved under an 8 min exposure to 1 sun) is 65.5% at a λ_{max} of 475 nm. The modulation at 550 nm for the same film is 55% and at NIR wavelengths of 1400 and 1900 nm, the ΔT values are 54 and 45% respectively. For the pristine V_2O_5 film, the magnitudes of transmission modulation are lower. At photopic wavelengths of 475 and 550 nm, the values are 36 and 31%. Even at NIR wavelengths, the modulation does not decrease much. Since both the hybrid and pristine oxide film are able to retain high values of optical modulation even in the NIR region, it is obvious that in addition to being capable of modulating visible wavelengths, the films can modulate NIR or heat radiation also efficiently. The role of PEDOP in increasing the conductivity of the V_2O_5 film, tends to promote electron transport in the oxide which in turn, is responsible for a greater uptake of sodium ions from the electrolyte, thus leading to a larger optical contrast, for the same duration of illumination. The pristine PEDOP film did not exhibit any change in transmittance as a function of illumination, perhaps due to a low thickness, or an insufficient electronic current to trigger a color change. As far as we know, there no reports on photo-induced color transitions reported for PEDOP or V_2O_5, but for a PEC with poly(3,3-diethyl-3,4-dihydro-2*H*-thieno-[3,4-*b*][1,4]dioxepine) (PProDot-Et_2) coupled with an organic dye sensitized TiO_2 film, a maximum ΔT of 33.7% was achieved.[34]

The solar cell parameters for the photovoltaic cells with the following configuration: CdS/TiO_2/Na_2S/V_2O_5 or PEDOP or PEDOP/V_2O_5 are provided in Table S1 (ESI†). We observed that the cell with pristine PEDOP as the counter electrode showed the highest efficiency, possibly because of the highest electronic conductivity compared to pristine V_2O_5 or the PEDOP/V_2O_5 hybrid. The large electronic conductivity of the counter electrode is beneficial for catalyzing the reduction of the oxidized electrolyte species, which leads to higher efficiency. Surprisingly, the cell with the hybrid as the counter electrode and the cell with V_2O_5 as counter show nearly equivalent efficiencies of 1.4%. The cell with hybrid shows a higher short circuit current density and a lower open circuit voltage compared to the cell with pristine V_2O_5 as counter electrode. The work function of the hybrid and V_2O_5 are 4.71 and 4.75 eV and these values are higher than the work function of PEDOP (4.65 eV) and these values are represented in the energy band diagram of the cell shown in Fig. 5d. Since the PEDOP based solar cell delivered the highest efficiency, the contribution from a favorable shallower work function along with its' high conductivity cannot be ruled out. A lower work function, as obtained for pristine PEDOP compared to the hybrid and the oxide, possibly also aids in rapid electron relay to the oxidized electrolyte species, which therefore leads to better solar cell performance metrics for PEDOP.

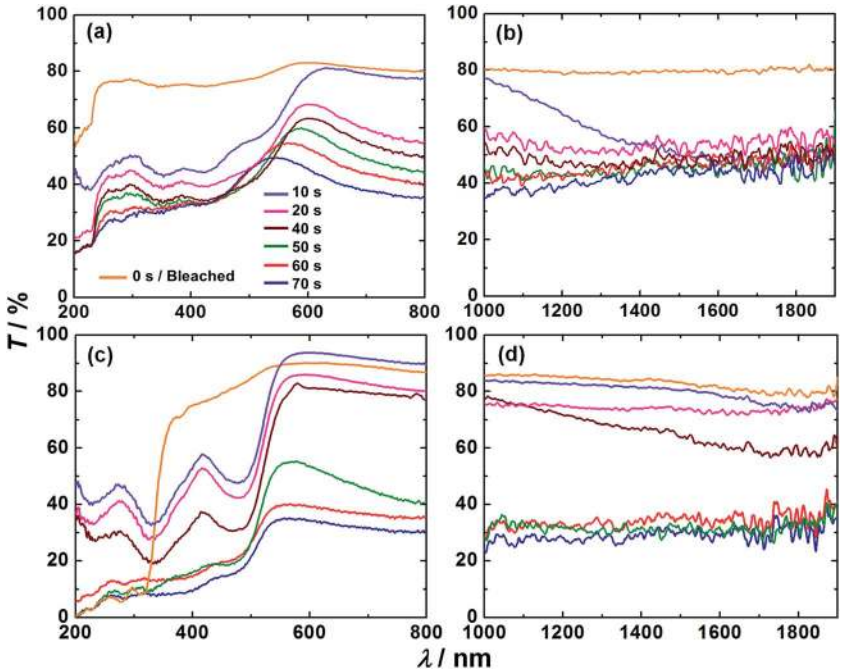

Fig. 8 Transmittance variation as a function of wavelength for the (a and b) pristine V_2O_5 nanobelts and (c and d) PEDOP/V_2O_5 hybrid as the coloring counter electrodes in the visible and NIR regions. The %*T* variation was recorded upon *x* s exposure of 1 sun illumination, $x = 0$, 10, 20, 40, 50, 60 and 70 s states in the following configurations: CdS/TiO_2/Na_2S/V_2O_5 in (a and b) and in the CdS/TiO_2/Na_2S/PEDOP/V_2O_5 in (c and d).

3.5. Charge–discharge characteristics

Cyclic voltammograms of pristine V_2O_5 or PEDOP or the PEDOP/V_2O_5 hybrid as working electrodes and graphite (Gr) as a counter electrode in a liquid electrolyte of 1 M $LiClO_4$ in PC (assembled in a two electrode configuration) at scan rates of 10, 50 and 100 mV s^{-1} are shown in Fig. 10. Pristine V_2O_5 showed featureless voltammograms at all the three scan rates, and the area under the curve increased with scan rate. In the CV plot recorded at 10 mV s^{-1}, pristine PEDOP shows a broad peak at −0.07 V in the anodic branch, corresponding to doping by perchlorate anions leading to the formation of the oxidized polymer. In the reverse sweep, a peak at −0.67 V is observed, which corresponds to the dedoping of perchlorate ions and formation of neutral PEDOP. Slight positional shifts in the anodic/cathodic peaks were observed at higher scan rates. For the PEDOP/V_2O_5 hybrid (at $\nu = 100$ mV s^{-1}), a broad peak is observed at +0.17 V in the anodic scan, and a wide peak was seen at −0.35 V in the cathodic scan. The first peak is due to the simultaneous oxidation of V_2O_5 and PEDOP and the second peak is due to the reduction of V_2O_5 and PEDOP by simultaneous electron intercalation and anion extraction. The overall current densities in the cathodic and anodic branches are higher for the hybrid compared to the pristine samples.

Asymmetric supercapacitor cells with the following configurations: V_2O_5–Gr, PEDOP–Gr and PEDOP/V_2O_5–Gr cells were studied, for the corresponding symmetric cells produced lower specific capacitances compared to symmetric cells. A 1 M $LiClO_4$/PC solution was used as the electrolyte. Further, asymmetric supercapacitors compared to symmetric capacitors are expected to be better performers, for after designing a configuration with a reasonable matching of the cathode and the anode, a high energy density manifests due to the low capacitance of the negative electrode compared to the positive electrode.[35] The configuration of the asymmetric cells is shown in a schematic in Fig. 11a. The galvanostatic charge–discharge curves of V_2O_5–Gr, PEDOP–Gr and PEDOP/V_2O_5–Gr cells obtained at a fixed current density of 2 A g^{-1} over a potential range of ∼−1 to +1 V are shown in Fig. 11b. The charge/discharge times are different for each electrode, for a constant magnitude of applied current density, thus suggesting different specific capacitances. The specific capacitances (SCs) of the active electrodes were calculated from the discharge curve by using the following equation.

$$SC = I \times \Delta t/\Delta V \times m \quad (4)$$

In eqn (4), SC is the specific capacitance, I is the current applied for discharge, Δt is the time in seconds for discharge, ΔV is voltage window and m is mass of active material of the working electrode. The specific capacitance for the PEDOP/V_2O_5–Gr cell is 224.5 F g^{-1} (212.18 s × 2 A g^{-1}/1.89 V) in comparison to a SC of 36.9 F g^{-1} (35 s × 2 A g^{-1}/1.895 V) achieved for pristine V_2O_5 and 68 F g^{-1} (64.6 s × 2 A g^{-1}/1.9 V) obtained for pristine PEDOP based cells. The voltage window offered by the active material (PEDOP/V_2O_5 or PEDOP or V_2O_5) is also rather wide, it is ∼1.9 V, in comparison to a typical voltage window of ∼1 V, reported for pseudocapacitive polymer/oxide – composites.[36,37] The substantial difference in specific capacitance ongoing from the pristine polymer or V_2O_5 to the hybrid, shows that the synergistic effects of the two components

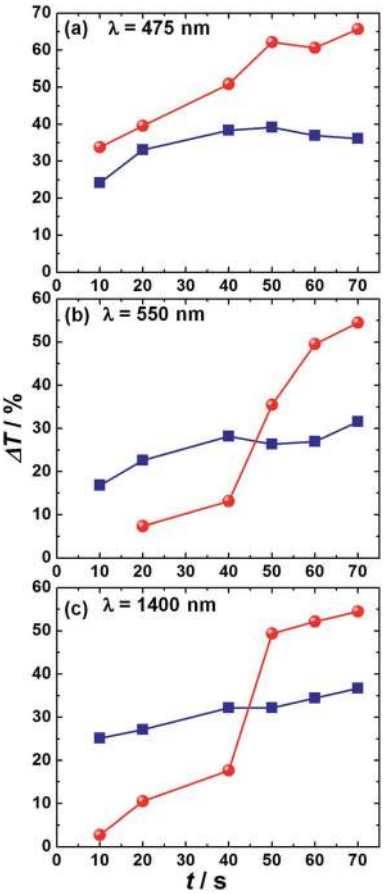

Fig. 9 Comparison of transmission modulation of pristine V_2O_5 nanobelts (■) and PEDOP/V_2O_5 hybrid (●) films at monochromatic wavelengths of (a) 475, (b) 550 and (c) 1400 nm. ΔT values were calculated using the transmittance in the corresponding bleached states ($x = 0$ s or open circuit condition shown in Fig. 7) as reference.

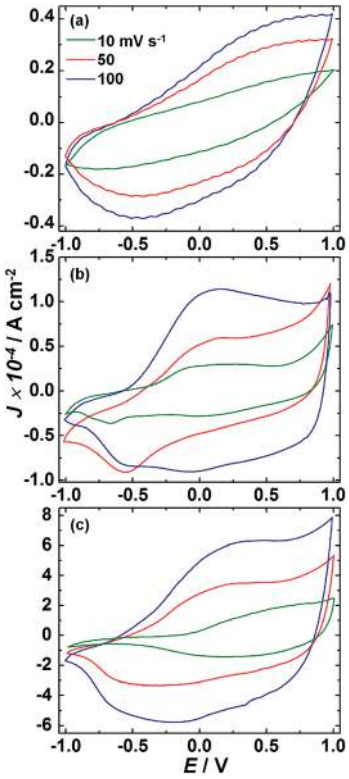

Fig. 10 Cyclic voltammograms of (a) V_2O_5–Gr, (b) PEDOP–Gr and (c) PEDOP/V_2O_5–Gr based two electrode cells recorded at scan rates of 10, 50 and 100 mV s^{-1}, in a 1 M $LiClO_4$/PC electrolyte.

are responsible for the observed enhanced SC of the hybrid. The high electronic conductivity of PEDOP improves the electron propagation capability of the electrode and the ability of V_2O_5 to store and release charge by undergoing simultaneous oxidation and reduction reactions. The rate capabilities of the V_2O_5–Gr, PEDOP–Gr and the PEDOP/V_2O_5–Gr cells were examined by recording the charge–discharge curves at different current densities of 1, 1.5 and 2 A g^{-1} (Fig. 11c–e). For V_2O_5 nanobelts, SC decreased from 76.9 to 36.9 F g^{-1} (~48% capacitance retention), and pristine PEDOP recovered 55% of its' specific capacitance, when the current density was raised from 1 to 2 A g^{-1}. The hybrid retained ~91% of its' capacitance when the current density was increased from 1 to 2 A g^{-1}, thus indicating a better rate performance compared to V_2O_5 or PEDOP. The cycling stabilities of the V_2O_5–Gr, PEDOP–Gr and the PEDOP/V_2O_5–Gr cells were determined by monitoring the variation of specific capacitance (obtained from the charge–discharge curves, at a current density of 2 A g^{-1}), as a function of galvanostatic charge–discharge cycles. At the end of 5000 charge–discharge cycles, the PEDOP/V_2O_5–Gr cell retained 90% of its' initial capacitance relative to ~15% and ~24% SC retention, achieved in the V_2O_5–Gr, PEDOP–Gr cells, thereby confirming the suitability of the hybrid for long life pseudocapacitors as well. The reason for capacity decline is volumetric expansion,[15] as ions intercalate and deintercalate on a repeated basis during cycling, the microstructure of the film is more efficient at accommodating the volume change due to ion ingress/egress in case of the hybrid compared to the pristine PEDOP or V_2O_5 films. In the hybrid, the conducting polymer buffers the volume change effectively, due to a highly entangled network of polymer chains, which is resistive to pulverization and disintegration from the electrode surface. Pristine PEDOP or V_2O_5, being sole entities, the tethering to the electrode surface and the ability to accommodate the volume expansion is poor and therefore capacity fade is fast. The high surface area and better electrolyte accessibility imparted by the V_2O_5 nanobelts coupled with the ability of PEDOP to store and release charge *via* doping/de-doping processes are responsible for the improved capacitive characteristics of the PEDOP/V_2O_5 hybrid. Energy and power densities of the electrodes were calculated using the following equations. Energy density $= Q \times \Delta V = I \times \Delta t \times \Delta V$, where Q is the charge per unit mass (in kg) available to the electrode when it is discharged from 100% state of charge to the cut-off voltage and Δt is the corresponding time taken for discharge. Power density $= I \times \Delta V$, where ΔV is the voltage range over which the current density (in A kg^{-1}) is applied. At a current density of 2 A g^{-1}, the hybrid showed an energy density of 222.7 W h kg^{-1} (212.5/3600 h $\times$ 2/0.001 A kg^{-1} $\times$ 1.89 V) at a power density of 3.78 kW kg^{-1} ((1.89 $\times$ 0.001) kV $\times$ 2/0.001 A kg^{-1}). Similarly, at the same

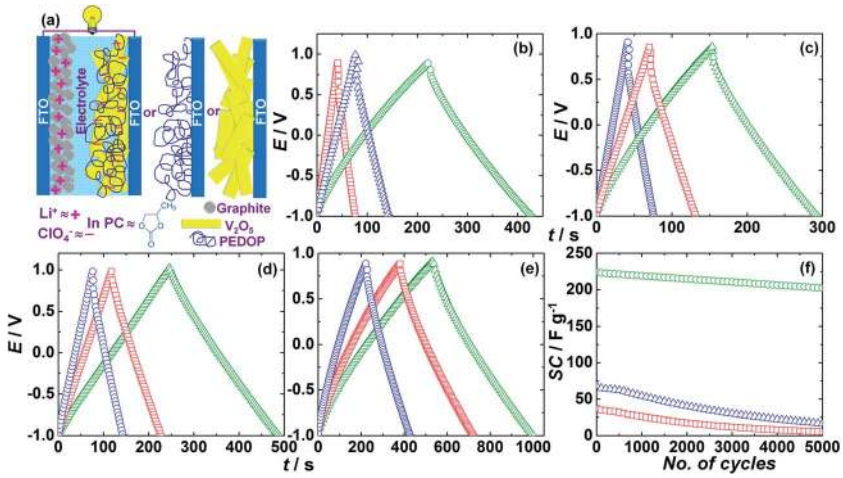

Fig. 11 (a) Schematic of asymmetric cells with a graphite film as the counter electrode and PEDOP/V_2O_5 or PEDOP or V_2O_5 as working electrode, and 1 M $LiClO_4$/PC as the electrolyte. Galvanostatic charge–discharge characteristics of (b) V_2O_5–Gr (□), PEDOP–Gr (△) and PEDOP/V_2O_5–Gr (○) based two electrode cells recorded at a constant current density of 2 A g^{-1} and rate capabilities of the (c) V_2O_5–Gr, (d) PEDOP–Gr, and (e) PEDOP/V_2O_5–Gr cells obtained at current densities of 1 (△), 1.5 (□) and 2 (○) A g^{-1}. (f) Specific capacitance (obtained at a constant current density of 0.1 A g^{-1}) *versus* number of cycles for V_2O_5–Gr (□), PEDOP–Gr (△) and PEDOP/V_2O_5–Gr (○) cells.

current density, the pristine polymer delivered an energy density of 68.2 W h kg^{-1} (64.6/3600 h × 2/0.001 A kg^{-1} × 1.9 V) at the same power density of 3.8 kW kg^{-1} ((1.9 × 0.001) kV × 2/0.001 A kg^{-1}). At the same current and power densities, pristine V_2O_5 showed an energy density of 36.8 W h kg^{-1} (35/3600 h × 2/0.001 A kg^{-1} × 1.895 V).

A comparison of energy storage characteristics with values from literature is provided here. In the past, a composite of RuO_2/PEDOT nanotubes prepared from an alumina template method delivered a power density of 20 kW kg^{-1} while maintaining 80% energy density (28 W h kg^{-1}) of its' maximum value.[38] In another report, a PEDOT nanotube based supercapacitor showed a high power density of 25 kW kg^{-1} and 80% energy density (5.6 W h kg^{-1}).[39] In another report, for MnO_2/PEDOT coaxial nanowires, prepared by co-electrodeposition in a porous alumina template, the coaxial nanowires preserved 85% of their specific capacitance (from 210 to 185 F g^{-1}) when the current density was raised from 5 to 25 mA cm^{-2}.[40] In another study, for a V_2O_5-reduced graphene oxide composite, a SC of 537 F g^{-1} was achieved at a current density of 1 A g^{-1}.[17] In yet another study, a SC of 316 F g^{-1} for the champion cell, was obtained for an interconnected porous network of V_2O_5, at a current density of 0.1 A g^{-1} corresponding to a voltage window of 1 V.[41] In the same study, authors obtained featureless CV plots, similar to our voltammograms observed for pristine V_2O_5. In another study, for stacked V_2O_5 nanosheets, a SC of 314 F g^{-1} was obtained at 0.5 A g^{-1} in an aqueous Na_2SO_4 electrolyte.[42] Authors obtained an energy density of 107 W h kg^{-1} for 3D architectures of V_2O_5, at a power density of 9.4 kW kg^{-1}.[42] For a V_2O_5/poly(pyrrole) composite, a large operational potential window of 2 V was observed.[18] Authors obtained an energy density of 82 W h kg^{-1} at a power density of 0.8 kW kg^{-1}. The SC of the composite was 412 F g^{-1}, at a current density of 0.0045 A cm^{-2}.[18] Our results for the PEDOP/V_2O_5 hybrid, in terms of the large operation potential window range (nearly 2 V), good cycling stability, as capacity reduces from 224 to 202 F g^{-1}, after 5000 charge–discharge cycles, and reasonably high energy density and power density demonstrate that the hybrid is a useful material for energy storage.

4. Conclusions

V_2O_5 nanobelts, 50 to 70 nm wide and several microns in length with a monoclinic crystalline structure, were synthesized by a hydrothermal route and a PEDOP layer was electropolymerized onto the oxide to yield a PEDOP/V_2O_5 hybrid film. The electronic conductivity of V_2O_5 nanobelts improved by 4-fold times upon integrating it with PEDOP and both V_2O_5 and the PEDOP/V_2O_5 hybrid exhibited green-red luminescence. By Kelvin probe force microscopy, the work function of the hybrid was deduced to be 4.71 eV, intermediate to that of the oxide and the polymer, which indicated its' suitability as counter electrode in solution processed solar cells. Photoelectrochromic cells were assembled with V_2O_5 nanobelts or PEDOP/V_2O_5 as the coloring counter electrodes and CdS/TiO_2 assembly as the photoactive electrode. The hybrid underwent deep coloration upon one sun illumination, with a maximum transmission modulation of 65% (λ = 475 nm) compared to a modulation of 36% at the same wavelength for the pristine V_2O_5 nanobelts, thus exemplifying the role of PEDOP in improving the optical contrast of V_2O_5. The hybrid was also able to retain this high optical modulation even at NIR wavelengths thereby validating its' suitability for solar powered smart windows, as the yellow to green switch is effected by photocurrent and not by an external bias. The suitability of the hybrid for pseudocapacitors was also demonstrated as it showed a specific capacitance of 224 F g^{-1}, which was 6 times greater than that shown by the pristine V_2O_5 nanobelts. The hybrid also exhibited a higher energy density of ~223 W h kg^{-1} relative to the pristine polymer/oxide, and demonstrated 90% capacitance retention, at the end of five

thousand redox cycles. The conducting polymer/oxide hybrid film is applicable to both solar powered electrochromic glass and high performance supercapacitors. Our study also opens up possibilities for integration of PEDOP with other electrochromic transition metal oxides for similar dual function materials.

Acknowledgements

Financial support from the Department of Science & Technology (DST/TM/SERI/2K12/11(G)) is gratefully acknowledged. One of us (RM) thanks to United Grants of Commission for JRF.

Notes and references

1 G. Terán-Escobar, J. Pampel, J. M. Caicedo and M. Lira-Cantú, *Energy Environ. Sci.*, 2013, **6**, 3088–3098.
2 L. Alibabaei, H. Luo, R. L. House, P. G. Hoertz, R. Lopez and T. J. Meyer, *J. Mater. Chem. A*, 2013, **1**, 4133–4145.
3 Q. Lu, J. G. Chen and J. Q. Xiao, *Angew. Chem., Int. Ed.*, 2013, **52**, 1882–1889.
4 J. T. Mefford, W. G. Hardin, S. Dai, K. P. Johnston and K. J. Stevenson, *Nat. Mater.*, 2014, **13**, 726–732.
5 Z. Tong, J. Hao, K. Zhang, J. Zhao, B. L. Su and Y. Li, *J. Mater. Chem. C*, 2014, **2**, 3651–3658.
6 M. Sathiya, A. S. Prakash, K. Ramesha, J. M. Tarascon and A. K. Shukla, *J. Am. Chem. Soc.*, 2011, **113**, 16291–16299.
7 J. Liu, H. Xia, D. Xue and L. Lu, *J. Am. Chem. Soc.*, 2009, **131**, 12086–12087.
8 H. Peng, W. Wu, C. Zhang, G. Li and K. Chen, *Mater. Lett.*, 2011, **65**, 3436–3439.
9 C. Xiong, A. E. Aliev, B. Gnade and K. J. Balkus Jr, *ACS Nano*, 2008, **2**, 293–301.
10 S. Wang, Z. Lu, D. Wang, C. Li, C. Chen and Y. Yin, *J. Mater. Chem.*, 2011, **21**, 6365–6369.
11 G. Gu, M. Schmid, P. W. Chiu, A. Minett, J. Fraysse, G. T. Kim, S. Roth, S. Kozlov, E. Munoz and R. H. Baughman, *Nat. Mater.*, 2003, **2**, 316–319.
12 K. Takahashi, Y. Wang and G. Cao, *Appl. Phys. Lett.*, 2005, **86**, 053102.
13 A. V. Murugan, B. B. Kale, C.-W. Kwon, G. Campet and K. Vijayamohanan, *J. Mater. Chem.*, 2001, **11**, 2470–2475.
14 A. V. Murugan, C. W. Kwon, G. Campet, B. B. Kale, A. B. Mandale, S. R. Sainker, C. S. Gopinath and K. Vijayamohanan, *J. Phys. Chem. B*, 2004, **108**, 10736–10742.
15 L. Shao, J. W. Jeon and J. L. Lutkenhaus, *Chem. Mater.*, 2012, **24**, 181–189.
16 C. Costa, C. Pinheiro, I. Henriques and C. A. T. Laia, *ACS Appl. Mater. Interfaces*, 2012, **4**, 5266–5275.
17 M. Li, G. Sun, P. Yin, C. Ruan and K. Ai, *ACS Appl. Mater. Interfaces*, 2013, **5**, 11462–11470.
18 M.-H. Bai, L.-J. Bian, Y. Song and X.-X. Liu, *ACS Appl. Mater. Interfaces*, 2014, **6**, 12656–12664.
19 L. Mai, F. Dong, X. Xu, Y. Luo, Q. An, Y. Zhao, J. Pan and J. Yang, *Nano Lett.*, 2013, **13**, 740–745.
20 X. Zhou, G. Wu, J. Wu, H. Yang, J. Wang and G. Gao, *Phys. Chem. Chem. Phys.*, 2014, **16**, 3973–3982.
21 Z. Su, C. Yang, C. Xu, H. Wu, Z. Zhang, T. Liu, C. Zhang, Q. Yang, B. Li and F. Kang, *J. Mater. Chem. A*, 2013, **1**, 12432–12440.
22 W. Chen, R. B. Rakhi and H. N. Alshareef, *Nanoscale*, 2013, **5**, 4134–4138.
23 Y. Zhao, J. Liu, Y. Hu, H. Cheng, C. Hu, C. Jiang, L. Jiang, A. Cao and L. Qu, *Adv. Mater.*, 2013, **25**, 591–595.
24 B. N. Reddy, M. Deepa and A. G. Joshi, *Phys. Chem. Chem. Phys.*, 2014, **16**, 2062–2071.
25 B. N. Reddy and M. Deepa, *Polymer*, 2013, **54**, 5801–5811.
26 C. L. Gaupp, K. Zong, P. Schottland, B. C. Thompson, C. A. Thomas and J. R. Reynolds, *Macromolecules*, 2000, **33**, 1132–1133.
27 Y. H. Kim, C. Sachse, M. L. Machala, C. May, L. Müller-Meskamp and K. Leo, *Adv. Funct. Mater.*, 2011, **21**, 1076–1081.
28 G. Leftheriotis, G. Syrrokostas and P. Yianoulis, *Solid State Ionics*, 2013, **231**, 30–36.
29 A. Cannavale, M. Manca, L. De Marco, R. Grisorio, S. Carallo, G. P. Suranna and G. Gigli, *ACS Appl. Mater. Interfaces*, 2014, **6**, 2415–2422.
30 J.-J. Wu, M.-D. Hsieh, W.-P. Liao, W.-T. Wu and J.-S. Chen, *ACS Nano*, 2009, **3**, 2297–2303.
31 C. Díaz-Guerra and J. Piqueras, *Cryst. Growth Des.*, 2008, **8**, 1031–1034.
32 Y. Hu, Z. Li, Z. Zhang and D. Meng, *Appl. Phys. Lett.*, 2009, **94**, 103–107.
33 P. N. Kumar, R. Narayanan, M. Deepa and A. K. Srivastava, *J. Mater. Chem. A*, 2014, **2**, 9771–9783.
34 C. Y. Hsu, K. M. Lee, J. H. Huang, K. R. Justin Thomas, J. T. Lin and K. C. Ho, *J. Power Sources*, 2008, **185**, 1505–1508.
35 C. Long, T. Wei, J. Yan, L. Jiang and Z. Fan, *ACS Nano*, 2013, **7**, 11325–11332.
36 Q. Guan, J. Cheng, B. Wang, B. Ni, G. Gu, X. Li, L. Huang, G. Yang and F. Nie, *ACS Appl. Mater. Interfaces*, 2014, **6**, 7626–7632.
37 I. Shakir, Z. Ali, J. Bae, J. Park and D. J. Kang, *Nanoscale*, 2014, **6**, 4125–4130.
38 R. Liu, J. Duay, T. Lane and S. B. Lee, *Phys. Chem. Chem. Phys.*, 2010, **12**, 4309–4316.
39 R. Liu, S. I. Cho and S. B. Lee, *Nanotechnology*, 2008, **19**, 215710.
40 R. Liu and S. B. Lee, *J. Am. Chem. Soc.*, 2008, **130**, 2942–2943.
41 B. Saravanakumar, K. K. Purushothaman and G. Muralidharan, *ACS Appl. Mater. Interfaces*, 2012, **4**, 4484–4490.
42 J. Zhu, L. Cao, Y. Wu, Y. Gong, Z. Liu, H. E. Hoster, Y. Zhang, S. Zhang, S. Yang, Q. Yan, P. M. Ajayan and R. Vajtai, *Nano Lett.*, 2013, **3**, 5408–5413.